Available online at http://geology.uaic.ro/auig/
Analele Stiintifice ale Universitatii "Al. I. Cuza" din Iasi
Seria Geologie 59 (1) (2013) 5–22

AUI
GEOLOGIE

The composition and source of the raw material of two stone axes of Late Bronze Age from Neamț County (Romania) - A Raman study

Nicolae Buzgar[1], Andrei Ionuț Apopei[1],Vasile Diaconu[2], Andrei Buzatu[1]

[1] "Al. I. Cuza" University of Iaşi, Department of Geology, Archaeoinvest Platform, Scientifical Research Laboratory, 20A Carol I Blv., 700505 Iaşi, Romania
[2] The History & Ethnography Museum of Târgu Neamț, Ștefan cel Mare Street 37, 615200 Tg. Neamț, Romania

Abstract

Two stone axes of Late Bronze Age from Moldova region (Romania) have been studied by Raman spectroscopy. The first axe (A1) belongs to the archaeological site Vînători (Neamț county). From a petrographic viewpoint, the sample is an andesite with pyroxenes and amphiboles, having a porphyric texture. The Raman study reveals the presence of plagioclase feldspar, pyroxene, hornblende, hematite and prehnite. The second artefact (A2) belongs to Topolița archaeological site (Grumăzești, Neamț county). Petrographically, the sample is a meladiorite with hornblende. Besides plagioclase and amphibole, Raman spectroscopy also identified titanite, quartz, epidote and hematite. On the surface it has a thin and transparent layer of black carbon. The Raman spectral lines of black carbon corespond to those of the highly disordered graphite due to the broaden *D* and *G* peaks and also due to the inclusion of *D2* band (~1630 cm^{-1}) in the broad *G* band (~1600 cm^{-1}).The black carbon uniform layer of the axe A2 was achieved by *firing* in a reducing *atmosphere.*

Keywords: artefacts, stone axes, Raman spectroscopy, black carbon layer.

Introduction

The two stone axes (Fig. 1) originate from sites specific to the Noua culture (Late Bonze Age), a manifestation which encompassed a large territory, from the middle and upper courses of the Nistru River to the east of Apuseni Mountains, and from the Ukranian Subcarpathian region to the south of the forest steppe region between the Siret and Prut rivers (Romania). Characteristic for this culture are numerous settlements situated on low-lying landforms, as well as an animal-based economy and necropoles dominated by inhumation. The Noua culture developed between the 15th and 12th centuries B.C. (Vulpe, 2001).

The first artefact (A1) was recovered in 2001, from the surface of a Noua culture settlement located in the Vânători-Neamț

Corresponding author's e-mail: nicolae.buzgar@uaic.ro

village, Neamţ County (Diaconu, 2007). The fragment analysed belongs to the upper part of an axe. It display a cylindrical edge, ending in a semi-spherical button, with a slightly arched profile (Diaconu, 2008). According to the typology proposed by Vulpe (1959), such axes are included in the B category of battle axes with cylindrical edge. Contextually, it could also have been the social symbol of a warrior. This particular stone axe is similar to other stone axes found in the archaeological sites of both the Noua culture and other Bronze Age cultures of the Eastern Carpathian space. Similar pieces have been identified in the Borodino treasure (Ucraina) (Kaiser, 1997). What should also be noted is that a similar piece, together with a bronze dagger of eastern origin, were also discovered in the settlement from which the fragment was retrieved (Dumitroaia, 1986).

The second piece (A2) was discovered in the Topoliţa village, Neamţ County, on the surface of a settlement from the Late Bronze Age (Diaconu, 2007, 2009). The item represents the lower half of a stone axe, possibly from the category of battle axes as well. The artifact distinguishes itself through a series of morphological details. Thus, on both surfaces, it displays a longitudinal embossed nervure, which probably imitates the casting seam of metallic axes in bivalved molds. Furthermore, in the area of the perforation used for fastening the axe handle, it presents a horizontal nervure, serving a decorative purpose as well. The profile is slightly arched and the fragment displays a series of nicks (Diaconu, 2009). Considering the fact that it was discovered in association with materials specific for the Noua culture, there are no doubts regarding its dating. Analogous pieces have been identified in the Moldova region (Niculică et al., 2004), as well as in the northern Pontic area (Zápotoký, 1966; Kaiser, 1997).

The purpose of the present study is to identify the petrographic types, as well as the origin of the raw materials, using Raman spectrometry.

Fig. 1 The A1 and A2 stone axes.

Analytical procedure

The Raman spectra were obtained with a Horiba Jobin-Yvon RPA-HE 532 Raman Spectrograph with a multichannel air cooled (– 70°C) CCD detector, using a wavenumber doubled Nd-Yag laser, 532 nm and 100 mW nominal power. The spectral resolution was 4 cm^{-1}, and the spectral range – between 200 and 3400 cm^{-1}. The Raman system includes a

"Superhead" fibre optic Raman probe for non-contact measurements, with a 50X LWD visible objective Olympus, NA = 0.50 WD = 10.6 mm. Sulphur and ciclohexane bands were used for the calibration of the frequencies of the Raman spectra. The data were acquired through 1–20 second exposure, 20–100 acquisitions, at a laser magnification of 70–100%. The close-up photos were taken using a Sony DSLR-A100 + Sony 3.5-5.6/18–70 mm.

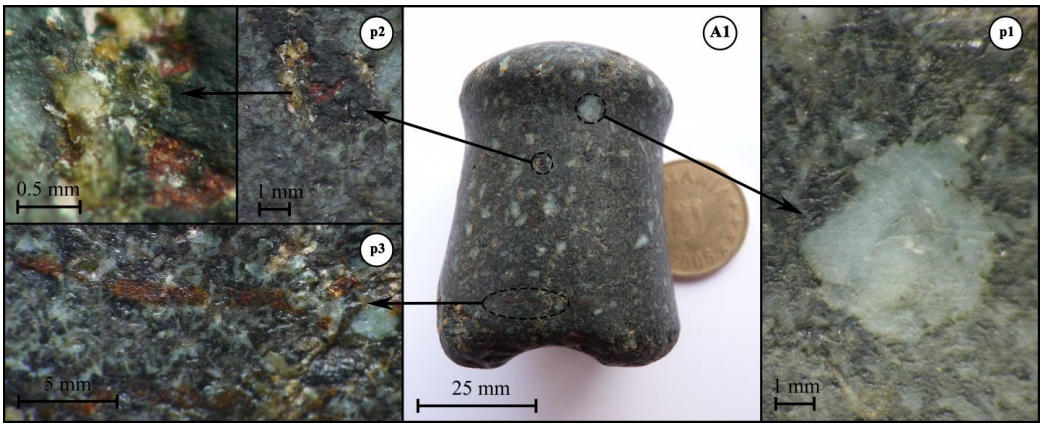

Fig. 2 The A1 artefact, close-up photos in three different points.

Results

The close-up photo of the A1 artefact (Fig. 2) reveals the presence of white feldspar (p1), black pyroxene and/or amphibole phenocrystals (p2, p3) and of a greenish gray groundmass (p2). It has a porphyritic texture. Scarce millimiter-sized crystalline agregates can be noticed, appearing as yellow to dark green and reddish-brown fractions constituing hydrothermal veinlets.

The Raman spectrum of the white feldspar phenocrystals displays the Raman bands characteristic for plagioclase feldspar, labradorite type. For the black phenocrystals, two different types of Raman spectra have been obtained: one corresponds to a monoclinic pyroxene (augite) and the other to an amphibole (hornblende). In the case of hydrothermal veinlets, the greenish mineral was identified as prehnite, while the red-brown mineral was found to be hematite.

The Raman spectrum obtained for the plagioclase phenocrystals display the main Raman feature of labradorite at the 510 cm^{-1} frequency (Fig. 3). The second Raman band in terms of intensity is observed at 483 cm^{-1}. These two bands can be assigned to the symmetric stretching mode of the T–O–T linkage (Freeman et al., 2008; Furukawa et al., 1981; Sharma et al., 1983), where T can be Si/Al (Al–O–Al linking in the tetrahedral network is forbidden, according to Lowenstein's rule (Loewenstein, 1954)). The Raman bands of labradorite in the 900–1200 cm^{-1} spectral domain are less well resolved owing to the broader band-widths.

A complete list of all the Raman bands observed in the labradorite of the present study, as well as other data from the literature (Downs, 2006; Mernagh, 1991) are provided in Table 1.

The Raman spectra of the black phenocrystals represented by augite and hornblende are shown in Figures 4 and 5. A summary of the assignment of the Raman bands is presented in Tables 2 and 3.

For the Raman spectrum of augite, the main Raman bands, located at 666 cm^{-1} and 1011 cm^{-1}, and assigned to the vibrational modes ν_s (Si–O_{br}) (O_{br} – bridging oxygen),

respectively to the ν_s (Si–O_{nbr}) (O_{nbr} – non-bridging oxygen) are in a good agreement with Buzatu and Buzgar (2010) and Huang et al. (2000). The bands assigned to the bending mode of O–Si–O bonds are located at around 560 cm^{-1}. The Raman bands which exhibit at lower frequencies (bellow 400 cm^{-1}) may be assigned to cation-oxygen vibrations.

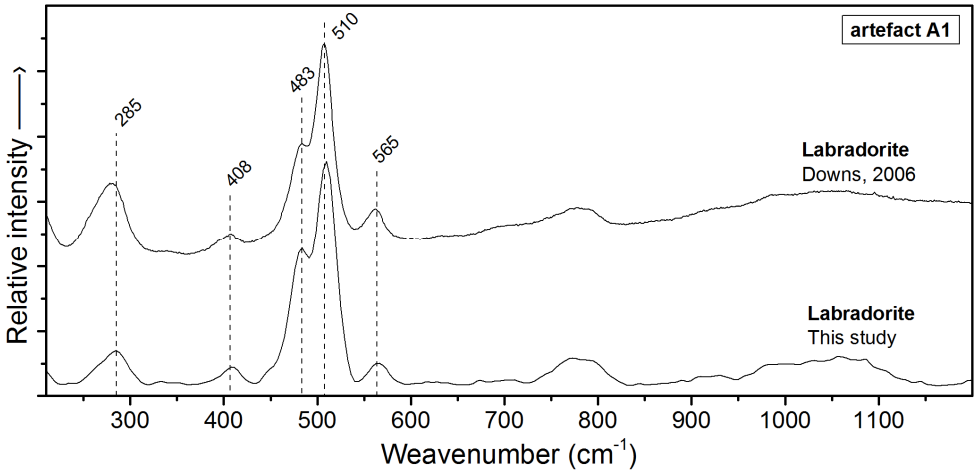

Fig. 3 The Raman spectrum of labradorite (present study) compared with reference Raman spectrum of labradorite from the RRUFF project (Downs, 2006).

Table 1. Assignment of the bands observed in the Raman spectrum of labradorite, in the 210–1200 cm^{-1} spectral domain

Band positions (cm^{-1})			Tentative assignments
Present study	Mernagh (1991)	Downs (2006)	
236, 266sh, 285	267, 281	259sh, 278	
333, 352	344, 354, 378	339	M–O
408	408, 419	396sh, 408	
449sh	–	–	ν_s(T–O–T)
483	484	484	ν_s(T–O–T)
510	510	507	ν_s(T–O–T)
565	565	562	δ(O–T–O)
673, 705	–	706	δ(O–T–O)
745sh, 773, 791	–	745sh, 777	δ(O–T–O)
929, 984, 1059	927, 1059	927, 989, 1057	ν_{as}(T–O–T)

Abbreviations: ν–stretching; $_s$–symmetric; $_{as}$–asymmetric; δ–deformation; sh–shoulder; T can be Al/Si, Al–O–Al linking is forbidden (Lowenstein's rule).

In the case of the Raman spectrum of hornblende (Fig. 5), the main features are the peaks located at 670 cm^{-1} and around 1054 cm^{-1}, which can be assigned to the symmetric stretching (ν_s) of the Si–O_{br}–Si linkage and the asymmetric stretching (ν_{as}) of the Si–O_{br}–Si linkage.

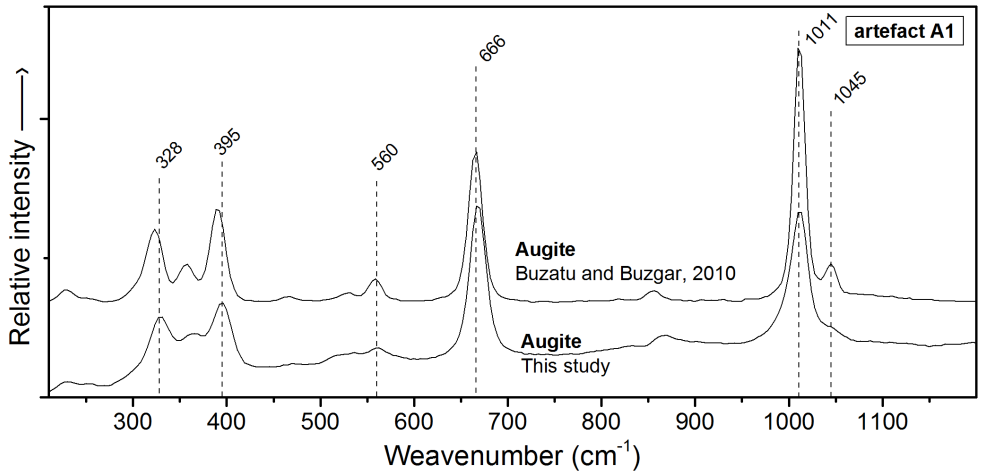

Fig. 4 The Raman spectrum of augite (present study) compared with reference Raman spectrum of augite (Buzatu and Buzgar, 2010).

Table 2 Assignment of the bands observed in the Raman spectrum of augite,in the 210–1200 cm^{-1} spectral domain

Band positions (cm^{-1})			Tentative assignments
Present study	Huang et al. (2000)	Buzatu and Buzgar (2010)	
230, 251	–	–	
328	323	324	M–O
365	352	352	
395	387	389	
470	461	477	δ(O–Si–O)
524, 535	508, 531	532	δ(O–Si–O)
560	556	555	δ(O–Si–O)
666	662	663	ν_s(Si–O_{br})
–	769	714, 771	ν_s(Si–O_{nbr})
–	–	816	ν_s(Si–O_{nbr})
831	862	853	ν_s(Si–O_{nbr})
868	–	878	ν_s(Si–O_{nbr})
–	–	896, 924	ν_s(Si–O_{nbr})
1011	1007	1006	ν_s(Si–O_{nbr})
1045	1038	1037	ν_s(Si–O_{nbr})
1088	–	1109	ν_s(Si–O_{nbr})

Abbreviations: ν–stretching; $_s$–symmetric; δ–deformation; sh–shoulder; O_{br}–bridging oxygen; O_{nbr}–non-bridging oxygen;T can be Al/Si, Al–O–Al linking is forbidden (Lowenstein's rule).

What should be pointed out is that the difference between the two Raman spectra of hornblende (Fig. 5, hornblende A1 and A2) consists in a minor shifting of the ν_1 band

towards higher frequencies (in the case of the reference spectrum, from 670 to 674 cm^{-1}). According to Apopei et al. (2011), this is due to the substitution of ^{IV}Si by ^{IV}Al in tetrahedral sites, which involves the presence of symmetric stretching of the Si–O_{br}–Al or the Al–O_{br}–Si. Taking into account the relationship between ^{IV}Si and ^{IV}Al atoms per formula unit (*apfu)* versus wavenumber suggested by Apopei et al. (2011), it can be assumed that the hornblende from the A1 artefact has a low ^{IV}Al content.

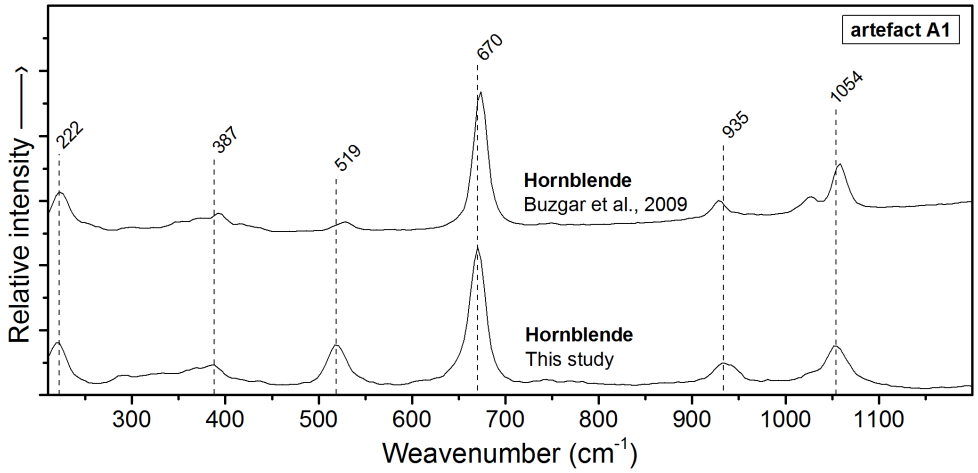

Fig. 5 The Raman spectrum of hornblende (present study) compared with reference Raman spectrum of hornblende (Buzgar et al., 2009).

Table 3 Assignment of the bands observed in the Raman spectrum of hornblende, in the 210–1200 cm^{-1} spectral domain

Band positions (cm^{-1})		Tentative assignments
Present study	Buzgar et al. (2009)	
222	222	lattice mode
290	298	
–	347	
370	373	M–OH
387	393	
412	416	
437	437	
519	527	$\delta(Si_4O_{11})$
670	674	ν_s(Si–O_{br}–Si)
935	929	ν_s(O–Si–O)
1028sh	1027sh	ν_{as}(Si–O_{br}–Si)
1054	1059	ν_{as}(Si–O_{br}–Si)

Abbreviations: ν–stretching; $_s$–symmetric; δ–deformation; sh–shoulder; O_{br}–bridging oxygen; T can be Al/Si, Al–O–Al linking is forbidden (Lowenstein's rule).

Prehnite is a phyllosilicate of Ca and Al with the ideal formula $Ca_2Al(AlSi_3O_{10})(OH)_2$ where the octahedral sites (*M1*) can contain along Al, also a limited amount of Fe. According to Akasaka et al. (2003), this amount of Fe^{3+} ranges from 0.003 to 0.425 *apfu*, while in other studies it varies but does not exceed 0.5 *apfu* (Downs, 2006; Liou et al., 1983; Surdam, 1969). Generally speaking, Fe^{3+} substitutes Al^{3+} in octahedral sites and scarcely in tetrahedral sites in some silicates; in the case of Fe-bearing prehnite, the ferric iron occurs only in octahedral sites where Al^{3+} is substituted by Fe^{3+} (Akasaka et al., 2003).

The Raman spectra of prehnite are characterized by several prominent peaks which are difficult to assign due to insufficient data currently available in the literature (Detrie, 2008). Figure 6 shows he most intense Raman band at 521 cm^{-1}, which can be assigned to the symmetric stretching of the $T–O_{br}–T$ linkage. This Raman band has one shoulder peak on each side, at 485 cm^{-1} and 541 cm^{-1}, respectively. The spectral region bellow 450 cm^{-1} is a more difficult to assign, since vibrational modes of M–O from octahedral sites where substitution of Al^{3+} by Fe^{3+} occur, translational and librational modes of OH groups, and also lattice modes which involves multi-atom movement are expected to arise in this spectral domain. A complete tentative assignment of the Raman bands is summarized in Table 4.

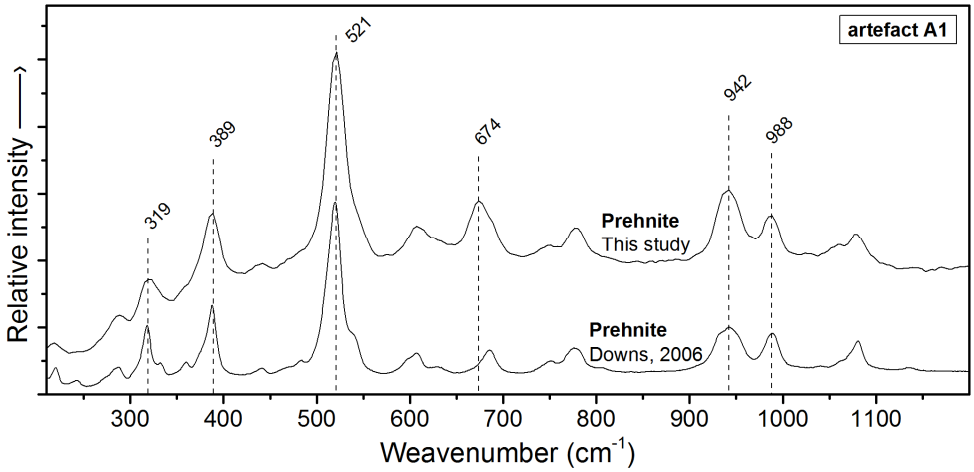

Fig. 6 The Raman spectrum of prehnite (present study) compared with reference Raman spectrum of prehnite from RRUFF project.

Bearing in mind the previous discussion about the variation of Fe^{3+} in octahedral sites and considering the Raman spectra of both R040047 prehnite with 0.43 Fe^{3+} *apfu* in octahedral sites, and R050410 prehnite with no Fe^{3+} content in octahedral sites (Downs, 2006), the Raman bands of both spectra overlay with small exceptions. The most notable difference is the 442 cm^{-1} band, which occurs in the Raman spectrum of prehnite with no iron (III) content. The presence of Fe^{3+} (substituting Al^{3+}) in R040047 prehnite causes the shifting of such Raman band from 442 cm^{-1} to a lower frequency, around ~ 430 cm^{-1}, as well as a shoulder at 416 cm^{-1} arises.

Figure 7 illustrates the Raman spectrum of hematite in the 210–1700 cm^{-1} spectral domain, with the characteristic peaks for hematite and black carbon. In the case of hematite, a lot of data have been provided both in the literature (Bikiaris et al., 1999; Boev et al., 2009; Buzgar et al., 2009; Downs, 2006; De Faria et al., 1997; Hernanz et al., 2006; Jubb and Allen, 2010; Marciuš et al., 2012; Minitti et al., 2005; Plümper and Putnis,

2009; Ren et al., 2011; Shim and Duffy, 2002; Ulubey et al., 2008; Wang et al., 1998) and across a wide range of disciplines (e.g. geosciences, archaeological studies etc.).

Table 4 Assignment of the bands observed in the Raman spectrum of prehnite, in the 210–1200 cm^{-1} spectral domain

Band positions (cm^{-1})			Tentative assignments
Present study	Downs (2006)	Detrie (2008)	
219	220, 242	215, 233	
288	287	275	lattice modes
319	318, 332sh	314	M–O;
360sh	360	361	translational and librational
389	388	375, 384, 397	motions of OH groups
442	441	461	
485sh	484sh	478, 495, 511	ν_s(T–O_{br}–T)
521	520	519	ν_s(T–O_{br}–T)
541sh	539sh	537	ν_s(T–O_{br}–T)
607	597sh, 607	605	δ(O–T–O)
628sh	630	–	δ(O–T–O)
674	685	–	δ(O–T–O)
751	751	751	δ(O–T–O)
777, 806sh	776, 806sh	777	δ(O–T–O)
942	942	932, 950	
988	989	987	stretching and bending
1061sh	1063sh	1059	of Si–O_{nbr}
1080	1081	1080	and T–O–T linkage
1139	1135	1136	

Abbreviations: ν–stretching; $_s$–symmetric; δ–deformation; sh–shoulder; O_{br}–bridging oxygen; O_{nbr}–non-bridging oxygen; T can be Al/Si, Al–O–Al linking is forbidden (Lowenstein's rule).

The 222, 292, 406, 495, 607, 1056, 1096 and 1193sh cm^{-1} Raman bands clearly indicate the presence of hematite. The weak Raman band at 659 cm^{-1} is linked to the partial transformation into magnetite under the laser beam, as first noticed by Bouchard (2001). Beattie and Gilson (1970) mention that the high power of the laser at the moment of the capture of the Raman spectrum makes most of the Raman lines corresponding to hematite to appear broadened and causes them to undergo a small shift to lower wavenumbers, as shown in Figure 7 and Table 5.

The most notable shifting can be observed in the case of the Raman band from 406 cm^{-1} to 411 cm^{-1}, which can be attributed eigher to the substitution of Fe^{3+} by other metal ions in the octahedral sites, or to the temperature of the sample under the high laser power (53.6 mW).

For the black carbon the main features are *D* and *G* bands at ~1360 $cm^{-1}$and ~1592 cm^{-1}, which are very broad and in a good agreement with literature data (Beattie and Gilson, 1970; Ferrari and Robertson, 2000; Ferrari and Robertson, 2004; Hernanz et al., 2006; Tunistra and Koenig, 1970; Wang et al., 1990). The Raman band of the hematite, located at 1318 cm^{-1}, overlapps *D* band of the black carbon (Fig. 7).

The A2 artefact displays an equigranular texture (Fig. 8). It contains white feldspar, black amphibole and reddish-brown titanite. The close-up photo revealed the presence of green epidote and brownish-red hematite, as well (p1, p2).

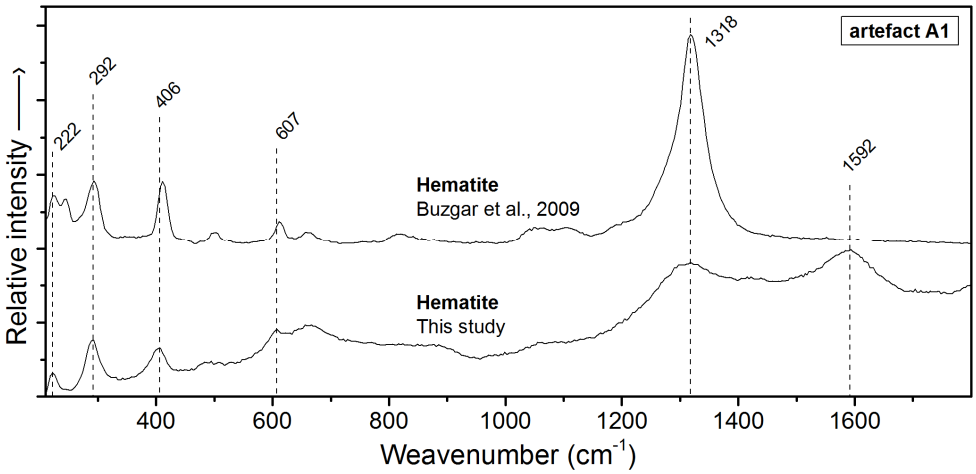

Fig. 7 Raman spectrum of hematite (present study) compared with reference Raman spectrum of hematite (Buzgar et al., 2009).

Table 5 Assignment of the bands observed in the Raman spectrum of hematite, in the 210–1700 cm^{-1} spectral domain.

Band positions (cm^{-1})		Tentative assignments
Present study	Buzgar et al. (2009)	
222	225	
–	245sh	
292	292	
406	411	
495	502	
543sh	–	hematite ($\alpha - Fe_2O_3$) vibrations
607	612	
659	659	
–	819	
1056	1053	
1096	1102	
1193sh	1192sh	
1318	1318	
~1360sh	–	*D* band of bc
1592	–	*G* band of bc

Abbreviations: sh–shoulder; bc–black carbon.

The Raman study pointed out the presence of oligoclase, hornblende, titanite, quartz, epidote and hematite. The entire artefact is covered with a thin, almost transparent carbon layer, giving it a dark to black tint, and also a characteristic glossy feature.

For the Raman spectrum of oligoclase (Fig. 9), two intense bands appear at 510 and 481 cm^{-1}. These bands are assigned to the symmetric stretching mode of the T–O–T linkage, where T

can be Si/Al (Al–O–Al linking is forbidden). A complete list of all the Raman bands observed in oligoclase, as well as their tentative assignments, is provided in Table 6.

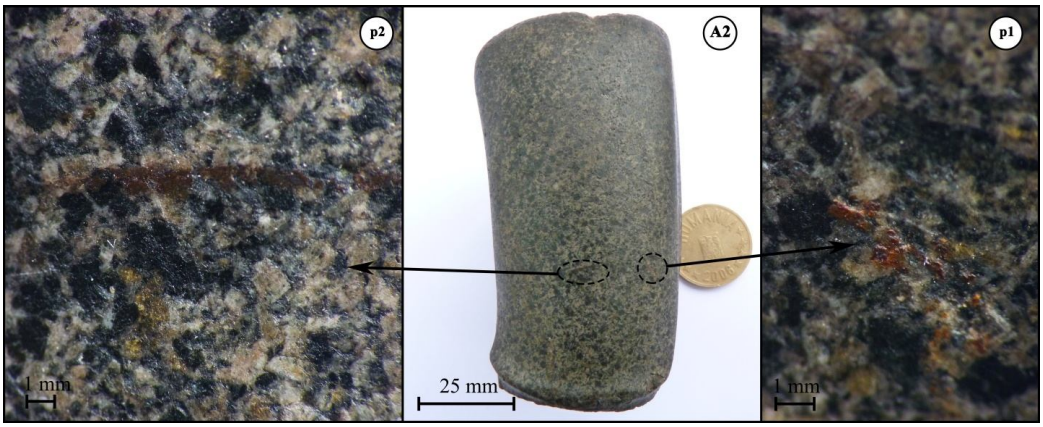

Fig. 8 The A2 artefact, close-up photos in two different points.

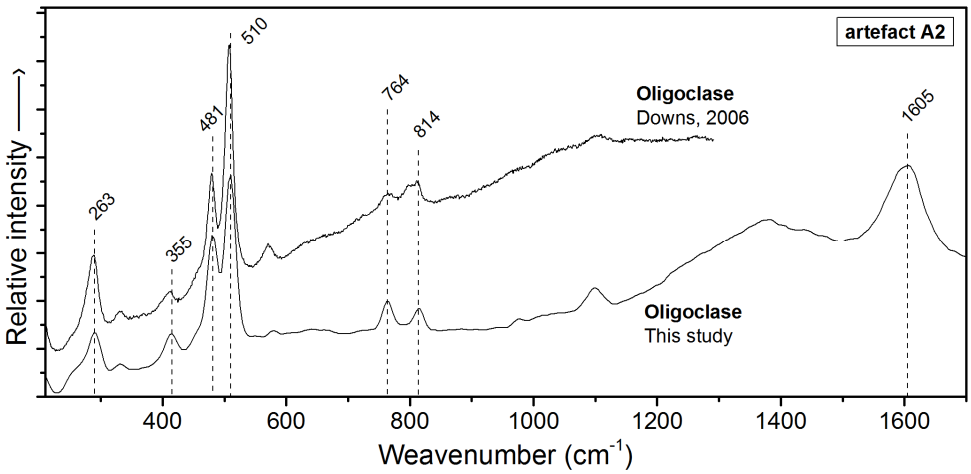

Fig. 9 Raman spectrum of oligoclase (present study) compared with reference Raman spectrum of oligoclase from RRUFF project.

The presence of black carbon (Fig. 9) is indicated by the spectral lines located at ~1382 and 1605 cm^{-1}, assigned to disordered graphitic *D*-band and to the graphitic *G*-band, respectively (Ferrari and Robertson, 2000).

The Raman spectrum of hornblende (Fig. 10) is dominated by a very strong sharp band at 668 cm^{-1} assigned to the symmetric stretching of the $S–O_{br}–Si$ linkage. The Raman bands which arise at higher frequencies (1030sh and 1054 cm^{-1}) are due to the asymmetric stretching of the $Si–O_{br}–Si$ linkage (Apopei et al., 2011; Apopei and Buzgar, 2010).The assignment of the Raman bands is summarized in Table 7.

Table 6 Assignment of the bands observed in the Raman spectrum of oligoclase, in the 210–1700 cm^{-1} spectral domain

Band positions (cm^{-1})			Tentative assignments
Present study	Mernagh (1991)	Downs (2006)	
290, 332, 415	283, 386	289, 331, 412	M–O
481	480	479	ν_s(T–O–T)
510	508	508	ν_s(T–O–T)
579	638	–	δ(O–T–O)
641, 667	729, 769, 780	571	δ(O–T–O)
724, 764, 814	832, 913	764, 811	δ(O–T–O)
978, 1043, 1099	988, 1107, 1183	1101	ν_{as}(T–O–T)
1382	–	–	*D* band of bc
1605	–	–	*G* band of bc

Abbreviations: ν–stretching; $_s$–symmetric; $_{as}$–asymmetric;δ–deformation; T can be Al/Si, Al–O–Al linking is forbidden (Lowenstein's rule); bc–black carbon.

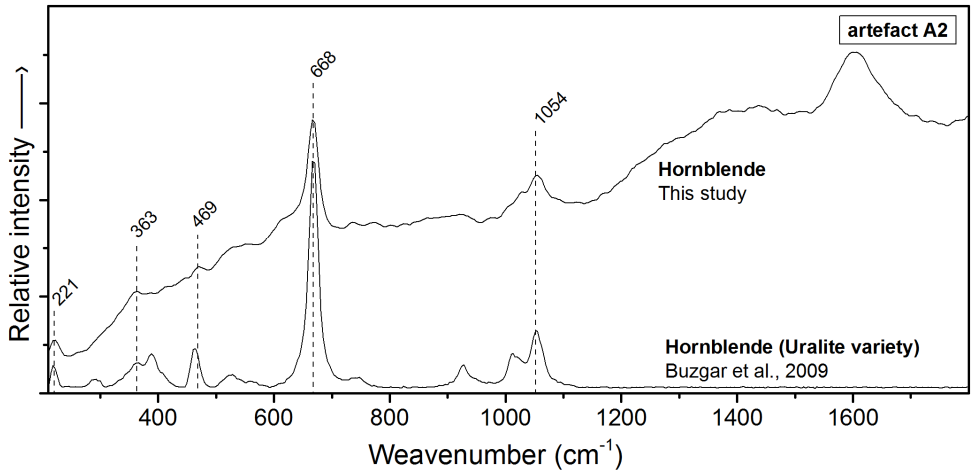

Fig. 10 The Raman spectrum of hornblende (present study) compared with reference Raman spectrum of hornblende (Buzgar et al., 2009).

The Raman spectrum of titanite (sphene, $CaTiSiO_4$ (O,OH,F)) obtained for the A2 artefact and the reference Raman spectrum of titanite (Buzgar et al., 2009) are shown in Figure 11, while the positions of the most prominent peaks are listed in Table 8.

Up to now, no rigorous band assignment has been carried out for the Raman spectrum of titanite in the 210–2300 cm^{-1} spectral region (Bismayer, 2000; Bismayer et al., 2010; Griffith, 1969; Heyns et al., 2000). Moreover, there are significant discrepancies between the positions of some Raman bands in these studies and in the present work. Given the lack of specific studies, the assignment of teh Raman bands to the vibrational modes is very complicated because of the substitutions from TiO_6 octahedra, SiO_4 tetrahedra and CaO_7 polyhedra.

Table 7 Assignment of the bands observed in the Raman spectrum of hornblende, in the 210–1800 cm^{-1} spectral domain.

Band positions (cm^{-1})		Tentative assignments
Present study	Apopei and Buzgar (2010)	
221	219, 292	lattice mode
363	364	M–O, where
–	388	M = Ca and Mg, Fe^{2+}
469	464	Q
551	526	$\delta(Si_4O_{11})$
668	668	$\nu_s(Si–O_{br}–Si)$
925	927	$\nu_s(O–Si–O)$
1030sh	1011	$\nu_{as}(Si–O_{br}–Si)$
1054	1053	
~1387	–	*D* band of bc
1601	–	*G* band of bc

Abbreviations: ν–stretching; $_s$–symmetric; δ–deformation; sh – shoulder; O_{br}–bridging oxygen; Q–quartz; bc–black carbon.

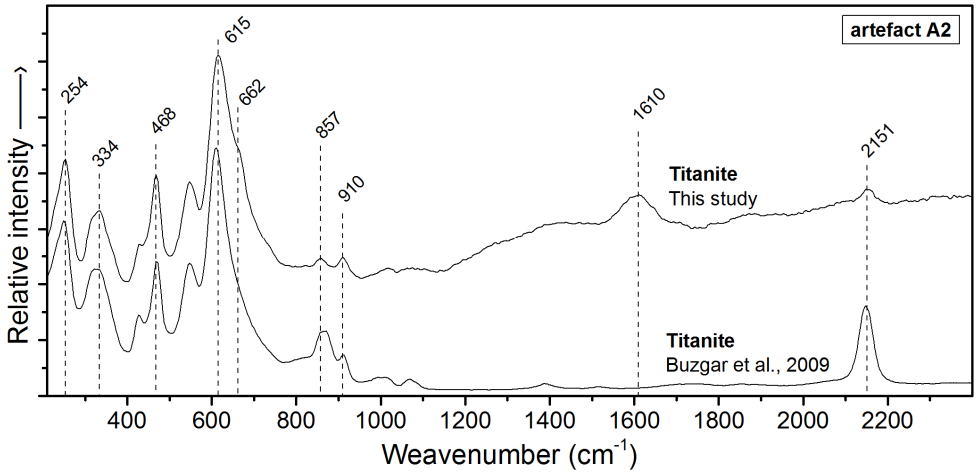

Fig. 11 Raman spectrum of titanite (present study) compared with reference Raman spectrum of titanite (Buzgar et al., 2009).

In octahedral sites, the Ti^{4+} can be substituted by Al^{3+}, Fe^{3+}, Fe^{2+}, Mg, Nb, Ta, V, Cr, while Ca can be substituted by Sr, Ba, Na, Mn or REE. In the case of tetrahedral sites, Si^{4+} can be substituted by Al^{3+}. Furthermore, a coupled substitution (Al, Fe^{3+}) + $(F,OH)^-$ = Ti^{4+} + O^{2-} occurs in titanite (Clark, 1974; Higgins and Ribbe, 1976).

From the Raman spectrum of titanite, one can easily distinguish a very strong and very sharp band at 615 cm^{-1}, which can be assigned to the symmetric stretching mode (ν_s) of Ti–O. This band has one shoulder around 662 cm^{-1} which can be due to the ν_s of the Al^{3+}/Fe^{3+}–O bonds, where, according to Higgins and Ribbe (1976), Ti^{4+} is partially substituted by Al^{3+}/Fe^{3+}, with Al^{3+} + Fe^{3+} not exceeding 30 mole percent, and Al^{3+} is usually predominant.

Table 8 Assignment of the bands observed in the Raman spectrum of titanite, in the 210–2300 cm^{-1} spectral domain.

Band positions (cm^{-1})		Tentative assignments
Present study	Buzgar et al. (2009)	
254	250	lattice mode;
334	327	Ca–O
429sh	427sh	$\delta(SiO_4)$
468	468	$\delta(SiO_4)$
547	548	$\delta(SiO_4)$
615	611	ν_s(Ti–O)
662sh	665sh	$\nu_s(Al^{3+}/Fe^{3+}–O)$
857	867	$\nu_s(SiO_4)$?
910	912	$\nu_s(SiO_4)$?
1016	1013	$\nu_{as}(SiO_4)$?
1390	1388	$\nu_{as}(SiO_4)$?
~1381	–	*D* band of bc
1610	–	*G* band of bc
2151	2148	*?*

Abbreviations: v–stretching; $_s$ – symmetric; $_{as}$ – asymmetric; δ–deformation; sh – shoulder; ?–questionable interpretation; bc–black carbon.

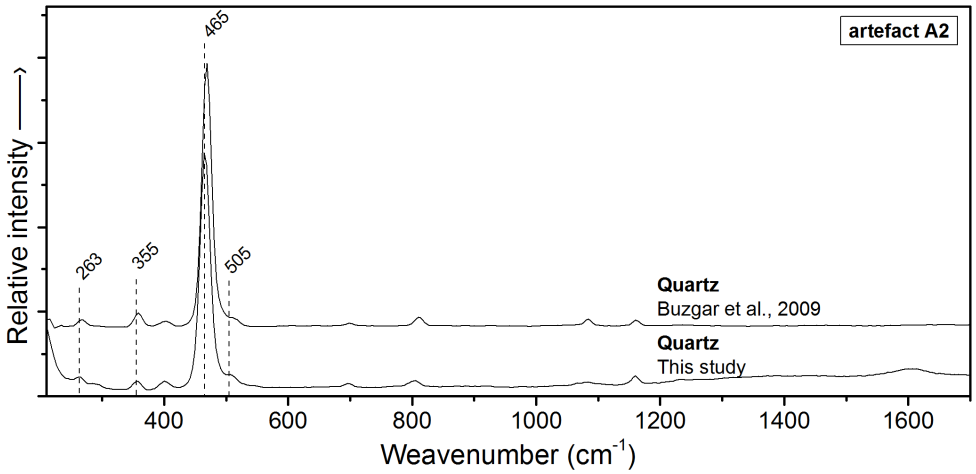

Fig. 12 Raman spectrum of quartz (present study) compared with reference Raman spectrum of quartz (Buzgar et al., 2009).

Taking into account the fact that, as a general rule, symmetric vibrations are more intense in Raman spectra, and asymmetric vibrations are more intense in IR spectra (Smith and Dent, 2005), the Raman bands which occur in the 800–1100 cm^{-1} spectral

domain can be divided into two regions, where SiO_4 tetrahedra exhibit two types of vibrations (Herzberg, 1945; Nakamoto, 1986): (i) between 800–950 cm^{-1} (ν_1) symmetric stretching vibrations of the SiO_4 tetrahedra are expected; and (ii) between 850–1200 cm^{-1} (ν_3) asymmetric stretching vibrations of SiO_4 tetrahedra are expected. For the low-frequency vibrational region, the Raman peaks between 400 and 550 cm^{-1} are due to the deformation modes of SiO_4 tetrahedra, while the 254 cm^{-1} band and the 334 cm^{-1} band can be assigned to lattice mode and Ca-O bonds, respectively. The presence of black carbon is given by the ~1381 cm^{-1} Raman band (*D* band) and the 1610 cm^{-1} Raman band (*G* band).

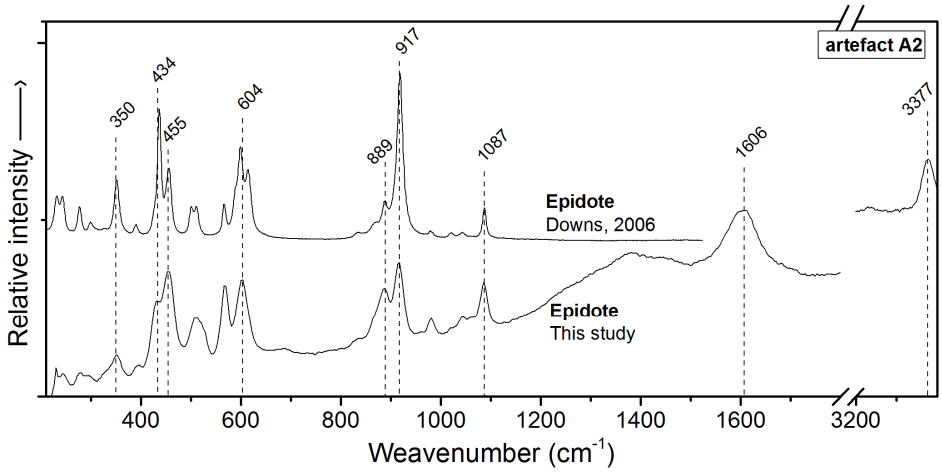

Figure 13. Raman spectrum of epidote (present study) compared with reference Raman spectrum of epidote from RRUFF project (Downs, 2006).

Figure 12 shows the Raman spectrum of quartz (present study) compared with the reference spectrum (Buzgar et al., 2009). Due to the symmetric stretching of Si–O–Si, a strong Raman band is positioned at 465(6) cm^{-1}. Weak bands are located at 263, 355 cm^{-1} (lattice modes), 805 cm^{-1} (bending of Si–O–Si) and 1086 cm^{-1} (asymmetric stretching SiO_4) (Kingma and Hemley, 1994; Krishnamurti, 1958; Williams, 1995).

So far, no studies have been carried out on epidote. Wang et al. (1994) reported the Raman spectrum of epidote, but did not provide further details about the assignment of the bands.

The Raman spectrum of epidote is characterized by strong bands at 434, 604, 917 and 3377 cm^{-1}, with a gap between the 650 and 850 cm^{-1} range, across which only two very weak bands, at 689 cm^{-1} and 834 cm^{-1}, arise (Fig. 13).Taking into consideration the many comprehensive IR studies regarding epidote (DellaVentura et al., 1996; Jovanovski et al., 2009; Langer and Raith, 1974; Liebscher, 2004), a tentative interpretation of the bands can be carried out, where most of the Raman bands are due to the symmetric stretching of the Si–O_{nbr} (at higher wavenumbers) and symmetric stretching of the Si–O_{br}–Si linkage (at lower wavenumbers). A complete list of Raman bands is provided in Table 9 with a tentative assignment.

The Raman spectrum of hematite obtained for the A2 artifact (Fig. 14) is very similar (in terms of band positions and intensities) with that obtained for the hematite from the A1 artifact (Fig.7).

All Raman spectra obtained for the A2

artifact display two broad bands of black carbon, one around 1360 cm^{-1} (the *D* band), assigned to the bond stretching of all pairs of sp^2 atoms in both rings and chains, and the other located around 1600 cm^{-1} (the *G* band), assignable to the breathing modes of sp^2 atoms in rings (Tunistra and Koenig, 1970; Ferrari and Robertson, 2000).

Table 9 Assignment of the bands observed in the Raman spectrum of epidote, in the 210–3400 cm^{-1} spectral domain

Band positions (cm^{-1})		Tentative assignments
Present study	Downs (2006)	
230, 245, 281, 296 331, 350, 396, 434 455, 510	232, 243, 277, 299 326, 352, 390, 437 456, 501, 510	lattice mode; M^{3+}–O (M^{3+} = Fe, Mn, Al)
566, 604, 689	566, 599, 615	ν_s Si–O_{br} of (SiO_4) & (Si_2O_7)
834, 889, 917, 981 1020, 1045, 1087	836, 868, 888, 919 979, 1020, 1043, 1087	ν_s Si–O_{nbr} of (SiO_4) & (Si_2O_7)
1381	–	*D* band of bc
1606	–	*G* band of bc
3377	3383	ν(OH)

Abbreviations: ν– stretching; $_s$ – symmetric; $_{as}$ – asymmetric; δ–deformation; sh–shoulder; O_{br}–bridging oxygen; O_{nbr}–non-bridging oxygen; ?–questionable interpretation; bc–black carbon.

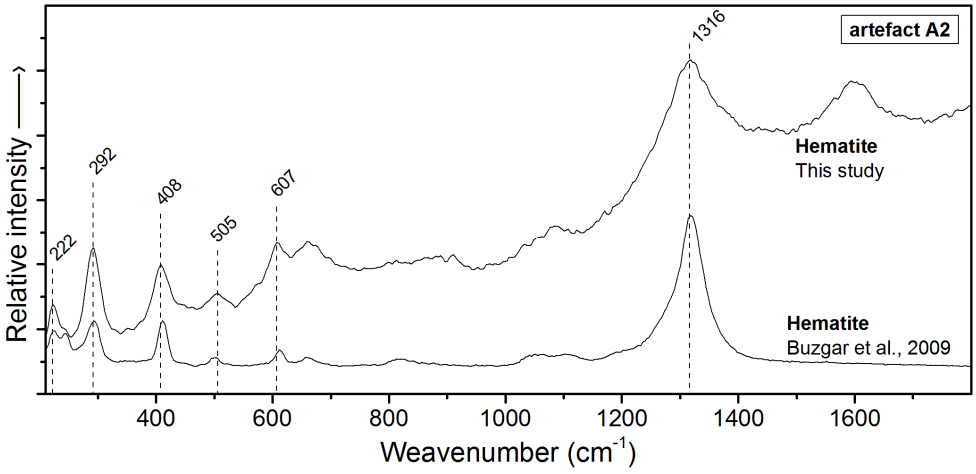

Fig. 14 Raman spectrum of hematite (present study) compared with reference Raman spectrum of hematite (Buzgar et al., 2009).

According to Tunistra and Koenig (1970), the intensity of the *D* band (~1360 cm^{-1}) is attributed to the particle size effect, and the slight shifting of the *G* band to a higher frequency is also correlated to the small crystal size. Furthermore, the increase in the D

and G bands' FWHM, as well as the decrease in the intensity ratios of the *D/G* band, indicate a growing degree of graphitisation (Tunistra and Koenig, 1970; Wang et al., 1990) of the carbonaceous material involved in the formation of the black carbon layer during the combustion process carried out in the absence of oxygen. Therefore, the even coating of the A2 axe with a glossy layer of black carbon was obtained through firing at high temperature, in a reducing environment. The coating of stone weapons and tools with a glossy layer of black carbon was evidence of the craftsmanship and spiritual power of the potter, the only one able to fire at high temperature and in a reducing environment. Whether the firing had a ritualistic character, or it was merely a means of manufacturing special weapons that acted as social symbols for their owners, is hard to say. We can only speculate on the purpose of this process of coating some of the weapons and tools with a glossy layer of black carbon.

Conclusions

Raman spectroscopy was successfully used for the identification of the major components present in both of the artifacts analyzed. For the A1 artifact, augite, hornblende, labradorite, hematite and prehnite minerals were identified. The augite and hornblende phenocrysts, together with the porphyritic texture, allow one to classify this raw material as an andesite with pyroxenes and amphiboles. This type of rock outcrops in the Eastern Carpathians, entering the structure of numerous Tertiary volcanoes.

For the A2 artifact, the texture, along with the main minerals (oligoclase, hornblende and high amount of titanite) identified through Raman spectroscopy, suggest that the item is a meladiorite with hornblende. The origin of the artifact lies in the Ditrău Alkaline Massif, situated in the Eastern Carpathians (Romania), approximately 100 km from the Vînători archaeological site, where the item was discovered. The presence of black carbonon the entire surface of the A2 axe suggests that the axe was burned intentionally, under reducing conditions, so as to make it shiny. A second hypothesis, according to which the axe was inflamed, cannot be taken into account.

References

Akasaka, M., Hideaki, H., Kuniaki, M., Ryozi, H., 2003. 57Fe Mössbauer and X-ray Rietveld studies of ferrian prehnite from Kouragahana, Shimane Peninsula, Japan. Journal of Mineralogical and Petrological Sciences, **98**, 31–40.

Apopei, A.I., Buzgar, N., Buzatu, A., 2011. Raman and infrared spectroscopy of kaersutite and certain common amphiboles. Analele Ştiinţifice ale Universităţii "Alexandru Ioan Cuza" Iaşi, Geologie, **57**, 2, 35–58.

Apopei, A.I., Buzgar, N., 2010. The Raman study of amphiboles. Analele Ştiinţifice ale Universităţii "Alexandru Ioan Cuza" Iaşi, Geologie, **56**, 1, 57–83.

Beattie, I.R., Gilson, T.R., 1970. The Single-crystal Raman Spectra of Nearly Opaque Materials. Iron(III) Oxide and Chromium(III) Oxide. Journal of the Chemical Society A, 1970, 980–986.

Bikiaris, D., Daniilia, S., Sotiropoulou, S., Katsimbri, O., Pavlidou, E., Moutsatsou, A.P., Chryssoulakis, Y., 1999. Ochre-differentiation through micro-Raman and micro-FTIR spectroscopies: application on wall paintings at Meteora and Mount Athos, Greece. Spectrochimica Acta, A, **56**, 1, 3–18.

Bismayer, U., 2000. Hard Mode Spectroscopy of Phase Transitions. Reviews in Mineralogy and Geochemistry, **39**, 265–283.

Bismayer, U., Paulmann, C., Groat, L., Zhang, M., 2010. Local Phenomena in matamict Titanite. Acta Physica Polonica A, **117**, 1, 74–77.

Boev, B., Jovanovski, G., Makreski, P., 2009. Minerals from Macedonia. XX. Geological Setting, Lithologies, and Identification of the Minerals from Ržanovo Fe-Ni Deposit. Turkish Journal of Earth Sciences, **18**, 631–652.

Bouchard-Abouchacra, M., 2001. Evaluation of Raman microscopy capacity of mineralogical and physico-chemical characterization of the archaeological materials: metals, stained glasses and pigments. Phd Thesis, Museé National d'Histoire Naturelle – MNHN Paris. (In French).

Buzatu, A., Buzgar, N., 2010. The Raman study of single-chain silicates. Analele Ştiinţifice ale Universităţii "Alexandru Ioan Cuza" Iaşi, Geologie, **56**, 1, 107–125.

Buzgar, N., Apopei, A.I., Buzatu, A., 2009. Romanian Database of Raman Spectroscopy (http://rdrs.uaic.ro).

Clark, A.M., 1974. A tantalum-rich variety of sphene. Mineralogical Magazine, **39**, 605–607.

De Faria, D.L.A., Venancio Silva, S., Oliveira, M.T., 1997. Raman microspectroscopy of some iron oxides and oxyhydroxides. Journal of Raman Spectroscopy, **28**, 11, 873–878.

Della Ventura, G., Mottana, A., Parodi, G.C., Griffin, W.I.,

1996. FTIR spectroscopy in the OH-stretching region of monoclinic epidotes from Praborna (St. Marcel, Aosta valley, Italy). European Journal of Mineralogy, **8**, 4, 655–665.

Detrie, T.A., 2008. Prehnite at the Atomic Scale: Al/Si Ordering, Hydrogen Environment, and High-Pressure Behavior. Msc, Virginia Tech, Blacksburg, VA.

Diaconu, V., 2007. Surface arhaeological reconnaissance in the area of Târgu Neamț town. Memoria Antiquitatis, **XXIV**, 87–119. (In Romanian).

Diaconu, V., 2008. Artefacts of polished rocks from Eneolithic și Bronze age descovered in the Neamț Basin. Carpica, **XXXVII**, 130–145. (In Romanian)

Diaconu, V., 2009. The settlement of the Noua culture from (Grumăzești, Neamț County). Suceava, **XXXIV-XXXV-XXXVI**, 171–183. (In Romanian)

Downs, R.T., 2006. The RRUFF Project: an integrated study of the chemistry, crystallography, Raman and infrared spectroscopy of minerals. Program and Abstracts of the 19th General Meeting of the International Mineralogical Association in Kobe, Japan, O03–13.

Dumitroaia, Gh., 1986. Sondajul arheologic de la Vânători-Neamț. Memoria Antiquitatis, **XII-XIV**, 15–27.

Ferrari, A.C., Robertson, J., 2000. Interpretation of Raman spectra of disordered and amorphous carbon. Physical Review B, **61**, 20, 14095–14107.

Ferrari, A.C., Robertson, J., 2004. Raman spectroscopy of amorphous, nanostructured, diamond-like carbon, and nanodiamond. Philosophical Transactions of The Royal Society A, **362**, 2477–2512.

Freeman, J.J., Wang, A., Kuebler, K.E., Jolliff, B.L., Haskin, L.A., 2008. Characterization of natural feldspars by Raman spectroscopy for future planetary exploration. The Canadian Mineralogist, **46**, 6, 1477–1500.

Furukawa, T., Fox, K.E., White, W.B., 1981. Raman spectroscopic investigation of the structure of silicate glasses. III. Raman intensities and structural units in sodium silicate glasses. The Journal of Chemical Physics, **75**, 7, 3226–3237.

Griffith, W.P., 1969. Raman studies on rock-forming minerals. Part 1. Orthosilicates and Cyclosilicates. Journal of the Chemical Society A, 1969, 1372–1377.

Hernanz, A., Gavira-Vallejo, J.M., Ruiz-Lopez, J.F., 2006. Introduction to Raman microscopy of prehistoric rock paintings from the Sierra de las Cuerdas, Cuenca, Spain. Journal of Raman Spectroscopy, **37**, 10, 1054–1062.

Herzberg, G., 1945. Molecular Spectra and Molecular Structure II. Infrared and Raman Spectra of Polyatomic Molecules. D. Van Nostrand Company, Inc., New Jersey.

Heyns, A.M., Harden, P.M., Prinsloo, L.C., 2000. Resonance Raman study of the high-pressure phase transition in chromium-doped titanite, CaTiOSiO4. Journal of Raman Spectroscopy, **31**, 8-9, 837–841.

Higgins, J.B., Ribbe, P.H., 1976. The crystal chemistry and space groups of natural and synthetic titanites. American Mineralogist, **61**, 878–888.

Huang, E., Chen, C.H., Huang, T., Lin, E.H., Xu, J., 2000. Raman spectroscopic characteristics of Mg-Fe-Ca pyroxenes. American Mineralogist, **85**, 473–479.

Jovanovski, G., Makreski, P., Kaitner, B., Boev, B., 2009. Silicate Minerals from Macedonia. Complementary Use of Vibrational Spectroscopy and X-ray Powder Diffraction for Identification and Detection Purposes. Croatica Chemica Acta, **82**, 2, 363-386.

Jubb, A.M., Allen, H.C., 2010. Vibrational Spectroscopic Characterization of Hematite, Maghemite, and Magnetite Thin Films Produced by Vapor Deposition. Applied Materials & Interfaces, **2**, 10, 2804–2812.

Kaiser, E., 1997. The hoard of Borodino: Critical observations on the Bronze age thesaurus from the north-east Schwarzmeergebeit. In Kommission bei R. Habelt, Bonn. (In German)

Kingma, K.J., Hemley, R.J., 1994. Raman spectroscopic study of microcrystalline silica. American Mineralogist, **79**, 269–273.

Krishnamurti, D., 1958. The Raman spectrum of quartz and its interpretation. Proceedings of the Indian Academy of Sciences A, **47**, 5, 276–291.

Langer, K., Raith, M., 1974. Infrared absorption spectra of Al-Fe(III) epidotes and zoisites, Ca2(Al1-pFe3+p)Al2O(OH)[Si2O7][SiO4]. American Mineralogist, **59**, 1249–1258.

Liebscher, A., 2004. Spectroscopy of Epidote Minerals. Reviews in Mineralogy & Geochemistry, **56**, 125–170.

Liou, J.G., Kim, H.S., Maruyama, S., 1983. Prehnite-Epidote Equilibria and their Petrologic Applications. Journal of Petrology, **24**, 321–342.

Loewenstein, W., 1954. The distribution of aluminum in the tetrahedra of silicates and aluminates. American Mineralogist, **39**, 92–96.

Marciuš, M., Ristić, M., Ivanda, M., Musić, S., 2012. Formation of Iron Oxides by Surface Oxidation of Iron Plate. Croatica Chemica Acta, **85**, 1, 117–124.

Mernagh, T. P., 1991. Use of the laser Raman microprobe for discrimination amongst feldspar minerals. Journal of Raman Spectroscopy, **22**, 8, 453–457.

Minitti, M.E., Lane, M.D., Bishop, J.L., 2005. A new hematite formation mechanism for Mars. Meteoritics & Planetary Science, **40**, 1, 55–69.

Nakamoto, K., 1986. Infrared Spectra of Inorganic and Coordination Compounds. 4th ed. Wiley, New York.

Niculică, B.P., Budui, V., Mareș, I., 2004. On some stone axes from the Bronze age descovered in the Sucevei Plateau. Suceava XXXIX-XXX, 267–315. (In Romanian).

Plümper, O., Putnis, A., 2009. The Complex Hydrothermal History of Granitic Rocks: Multiple Feldspar Replacement Reactions under Subsolidus Conditions. Journal of Petrology, **50**, 5, 967–987.

Ren, L., Huang, S., Fan, W., Liu, T., 2011. One-step preparation of hierarchical superparamagnetic iron oxide/graphene composites via hydrothermal method. Applied Surface Science, **258**, 3, 1132–1138.

Sharma, S.K., Simons, B., Yoder, H. S., 1983. Raman study of anorthite, calcium Tschermak's pyroxene, and gehlenite in crystalline and glassy states. American Mineralogist, **68**, 1113–1125.

Shim, S-H., Duffy, T.S., 2002. Raman spectroscopy of Fe2O3 to 62 GPa. American Mineralogist, **87**, 318–326.

Smith, E., Dent, G., 2005. Modern Raman Spectroscopy – A Practical Approach. John Wiley and Sons, England.

Surdam, R.C., 1969. Electron microprobe study of prehnite and pumpellyite from Karmutsen group, Vancouver Island, British Columbia. American Mineralogist, **54**, 256–266.

Tunistra, F., Koenig, J.L., 1970. Raman Spectrum of Graphite. The Journal of Chemical Physics, **53**, 1126–1130.

Ulubey, A., Fazlioglu, I., Erdogu, B., 2008. Pigment identification in hellenistic ceramics from the Tuz Golu region of Central Anatolia by confocal Raman spectroscopy. Ceramics - Silikaty, **52**, 201–204.

Vulpe, A., 1959. The Tufa deposit and the axes with cylindrical neck. Studii şi Cercetări de Istorie Veche, **10**, 2, 265–275. (In Romanian).

Vulpe, A., 2001. Perioada târzie a epocii bronzului. Istoria românilor, **I**, 272–287.

Wang, A., Han, J., Guo, L., Yu, J., Zeng, P., 1994. Database of Standard Raman Spectra of Minerals and Related Inorganic Crystals. Applied Spectroscopy, **48**, 8, 959–968.

Wang, A., Haskin, L.A., Jolliff, B.L., 1998. Characterization of mineral products of oxidation and hydration by laser Raman spectroscopy: Implications for in situ petrologic investigation on the surface of Mars. 28th Lunar Planetary Science Conference.

Wang, Y., Alsmeyer, D.C., McCreery, R.L., 1990. Raman Spectroscopy of Carbon Materials: Structural Basis of Observed Spectra. Chemistry of Materials, **2**, 557–563.

Williams, Q., 1995. Infrared, Raman and Optical Spectroscopy of Earth Materials. In Ahrens T.J. (Ed.). Mineral Physics and Crystallography: A Handbook of Physical Constants, American Geophysical Union, 291–302.

Zápotoký, M., 1966. Fight axes and fight axes culture. Památki Archeologické, **57**, 172–209. (In German).